PNAS
www.pnas.org

Supplementary Information for

Pressure-induced phase transitions and superconductivity in a black phosphorus single crystal

Xiang Li[a1], Jianping Sun[b,c1], Prashant Shahi[b,c], Miao Gao[d], Allan H. MacDonald[e], Yoshiya Uwatoko[f], Tao Xiang[b,g], John B. Goodenough[a2], Jinguang Cheng[b,c2], and Jianshi Zhou[a2]

[a] Materials Science and Engineering Program, The University of Texas at Austin, Austin, Texas 78712, USA; [b] Beijing National Laboratory for Condensed Matter Physics and Institute of Physics, Chinese Academy of Sciences, Beijing 100190, China; [c] School of Physics, University of Chinese Academy of Sciences, Beijing 100049, China; [d] Department of Microelectronics Science and Engineering, Faculty of Sciences, Ningbo University, Zhejiang 315211, China; [e] Department of Physics, The University of Texas at Austin, Austin, Texas 78712, USA; [f] Institute for Solid State Physics, The University of Tokyo, 5-1-5 Kashiwanoha, Kashiwa, Chiba 277-8581, Japan; [g] Collaborative Innovation Centre of Quantum Matter, Beijing 100871, China.

[1]X.L. and J.S. contributed equally to this work.
[2] To whom correspondence may be addressed. Email: jgoodenough@mail.utexas.edu, jgcheng@iphy.ac.cn, jszhou@mail.utexas.edu.

1. Growth of single-crystal black phosphorus.

We have prepared single crystals of black phosphorus (BP) with a Walker-type multianvil module (Rockland Research Co.) (1). The starting material of red phosphorus powder was pressed into a conical Lava crucible, which was asymmetrically placed into a graphite heater in order to achieve a temperature gradient during the crystal growth. The sample was heated up to 1473 K at 2 GPa for 2 hours and then slowly cooled down to 773 K at a rate of 100 K/hour before quenching to the room temperature.

2. Magneto-transport measurements with the palm cubic-anvil high pressure apparatus.

Magneto-transport properties on the BP single crystal under hydrostatic pressures up to 15 GPa were measured by using a "Palm" cubic anvil apparatus in the Institute of Physics, Chinese Academy of Sciences (2). A standard four-probe configuration was used for all the resistivity measurements. The BP single crystal was suspended by four ϕ20 μm golden wires in a Teflon capsule, which is filled with the glycerol pressure transmitting medium (PTM) and located in the center of a MgO cubic gasket. Hydrostatic pressure is generated by compressing the cubic gasket with six tungsten-carbide (WC) anvils from three orthogonal directions. We employed the WC anvils of 4×4 mm^2 top to generate pressures up to 8 GPa, and 2.5×2.5 mm^2 top to 15 GPa. Such a three-axis compression together with the adoption of liquid PTM ensures excellent pressure homogeneity. During the magneto-transport measurements, the minimum pressure for the palm cubic-anvil apparatus is about 1 GPa since a sufficient loading force is needed to seal the cell. The electrical current was flowing within the *a*-*c* plane of the A17 phase (the puckered honeycomb layer), and the magnetic field was fixed along the orthorhombic *b* axis (perpendicular to the puckered honeycomb layer). We have measured the field dependence of resistivity $\rho^{+}(H)$ from 0 to 8.5 T and $\rho^{-}(H)$ from 0 to -8.5 T, and then obtained the longitudinal magneto-resistivity $\rho_{xx}(H) = [\rho_{xx}^{+}(H) + \rho_{xx}^{-}(H)]/2$ and Hall resistivity $\rho_{xy} = [\rho_{xy}^{+}(H) - \rho_{xy}^{-}(H)]/2$ in order to remove the mutual influences.

3. Thermoelectric measurements performed in zero field under high pressure with a piston-cylinder device.

The temperature dependence of resistivity $S(T)$ under H = 0 T at various pressures is shown in Fig. S1. *S(T)* in a semiconductor could exhibit a maximum (S_{max}) at T_{max} which is proportional to the energy gap (E_g) via the relationship (3): $S_{max} \sim E_g/2eT_{max}$, . This behavior has been observed in BP at P < 1.0 GPa. We can estimate the energy gap E_g = 0.14(2) eV under ambient pressure, which is close to the previous results (4). With increasing pressure up to 1.2 GPa, T_{max} moves to a lower temperature, implying a reduction of the band gap under pressure. The band gap can be also derived from the resistivity. Correspondingly, the gap reduces under high pressure in the same way as that

from the thermoelectric power measurement under pressure.

The activated temperature dependence of S(T) at $T > T_{max}$ for $P < 1.0$ GPa is consistent with the semiconductor behavior in the resistivity at low temperatures under corresponding pressures. On crossing the critical pressure $P_c \sim 1.0$ GPa, S(T) near room temperature changes dramatically from $dS/dT < 0$ to $dS/dT > 0$ on top of a continuous reduction of the magnitude under pressure. A $dS/dT > 0$ at $P \geq 1.0$ GPa is compatible to the Mott diffuse formula for a metal. Generally speaking, the thermoelectric power reflects the imbalance of the energy dependence of conductivity crossing the Fermi level; therefore it may reveal any subtle change of the Fermi surface. The Lifshitz transition has been believed to be applicable in the pressure-induced semiconductor-semimetal transition. Specifically, tips of two Dirac cones are touching at the transition. The Dirac Fermions are massless and should have a vanishing thermoelectric power. The S(P) of BP is reduced on crossing the Lifshitz transition, but is far from vanishing. These observations indicate that although the Lifshitz transition is manifested in the thermoelectric power, carriers near the Fermi energy are not Dirac-like, at least within an energy range of kT.

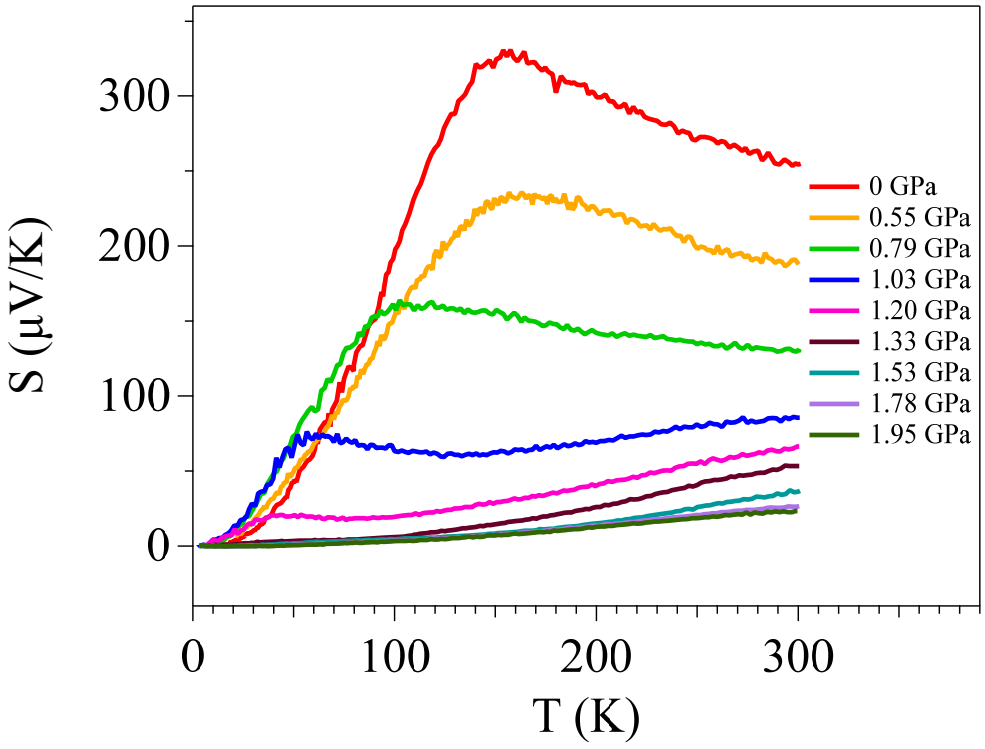

Fig. S1 (Color online) Thermoelectric power as a function of temperature under $H = 0$ T below 2 GPa.

3. Single-crystal X-ray structural study under high pressure

Single-crystal X-ray diffraction (SXRD) under pressure was performed on a BP crystal with a diamond anvil cell (DAC) mounted on a Bruker P4 diffractometer with Mo K-alpha radiation (λ = 0.71069 Å) at room temperature. The culet size of diamond anvil is 0.5 mm. The sample was loaded in a 0.25 mm hole drilled in a preindented stainless steel gasket. The pressure can be determined according to the peak position of the gasket which has been calibrated against the gold pressure manometer. As shown in Fig. S2, the diffraction was collected with an image plate placed at 152 mm behind the sample and integrated into intensity versus 2θ with a software Fit2d. The setup provides an X-ray access along the *b* axis and perpendicular to the *ac* plane of the A17 phase.

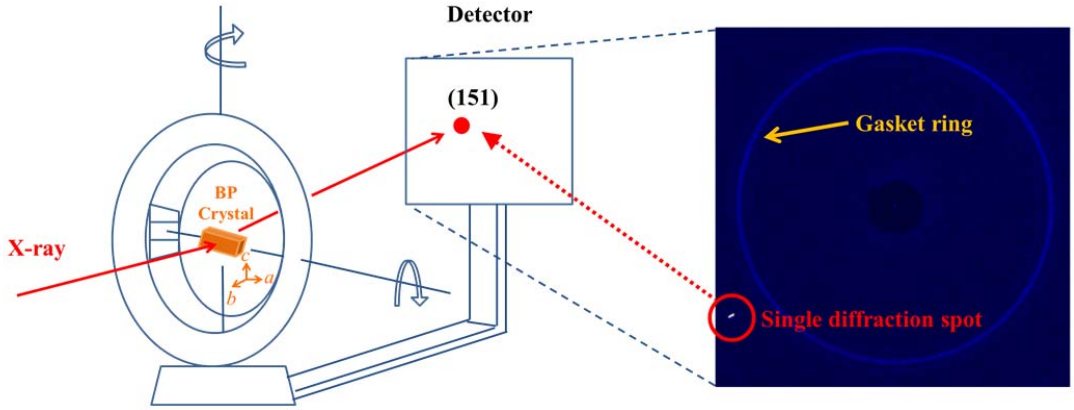

Fig. S2 (Color online) A schematic drawing of single-crystal X-ray diffraction and a single diffraction spot collected by an image plate as the detector.

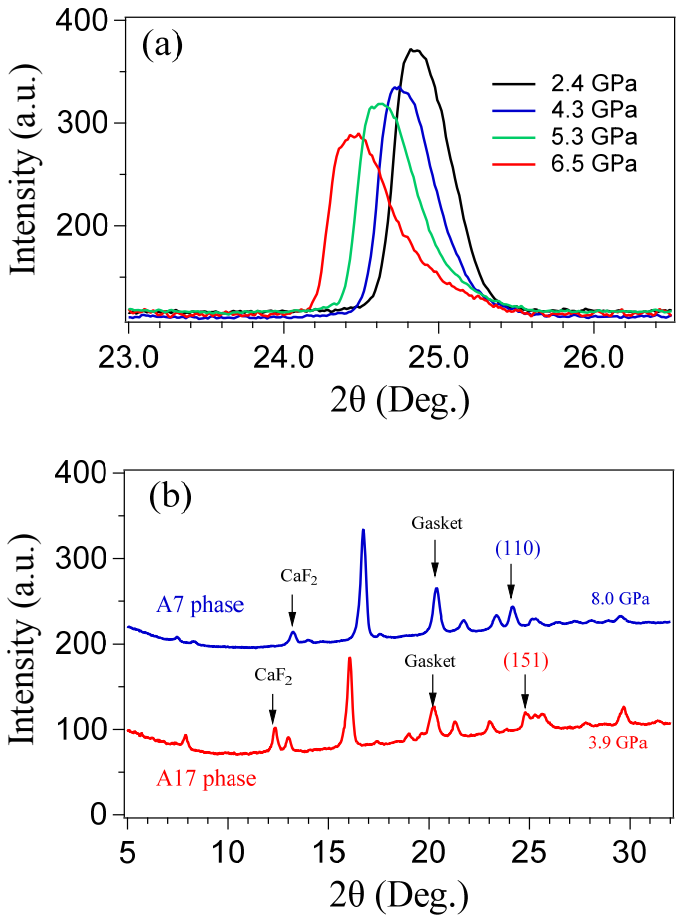

Fig. S3 (Color online) (a) Single-crystal X-ray diffraction patterns under high pressure; (b) Powder X-ray diffraction patterns measured with a DAC, in which the sample was loaded in a 0.25 mm hole drilled in a preindented stainless steel gasket, and CaF_2 was used as the pressure manometer.

We found a single spot was collected by the detector at the 2θ angle of ~25° (d ~ 1.65 Å), determined as the (151) plane in the A17 phase and (110) plane in the A7 phase. Fig. S3 shows the peak shifting towards lower angles, which arises from a tiny tilting of the crystal by pressurizing. Because of the X-ray diffraction configuration described above, to fulfill the Bragg condition $2d_{hkl}sin\theta_{hkl} = \lambda$ in both phases, the frame of the A7 structure has to be reoriented as shown in Fig. S4, which is consistent with previous theoretical prediction (5).

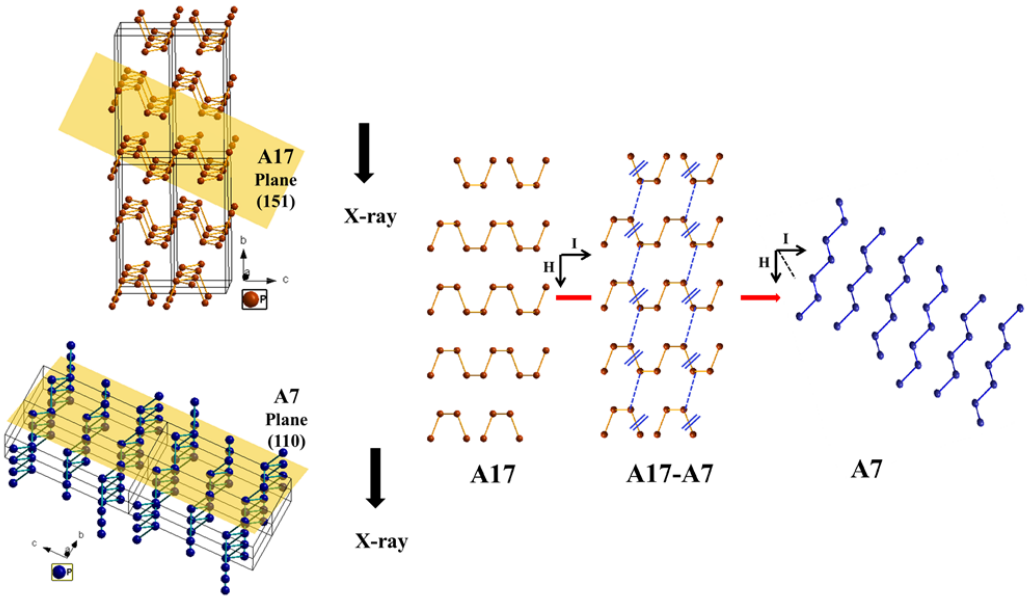

Fig. S4 (Color online) Reconstructing process of the A7 phase.

4. Quantum Shubnikov–de Haas (SdH) oscillations

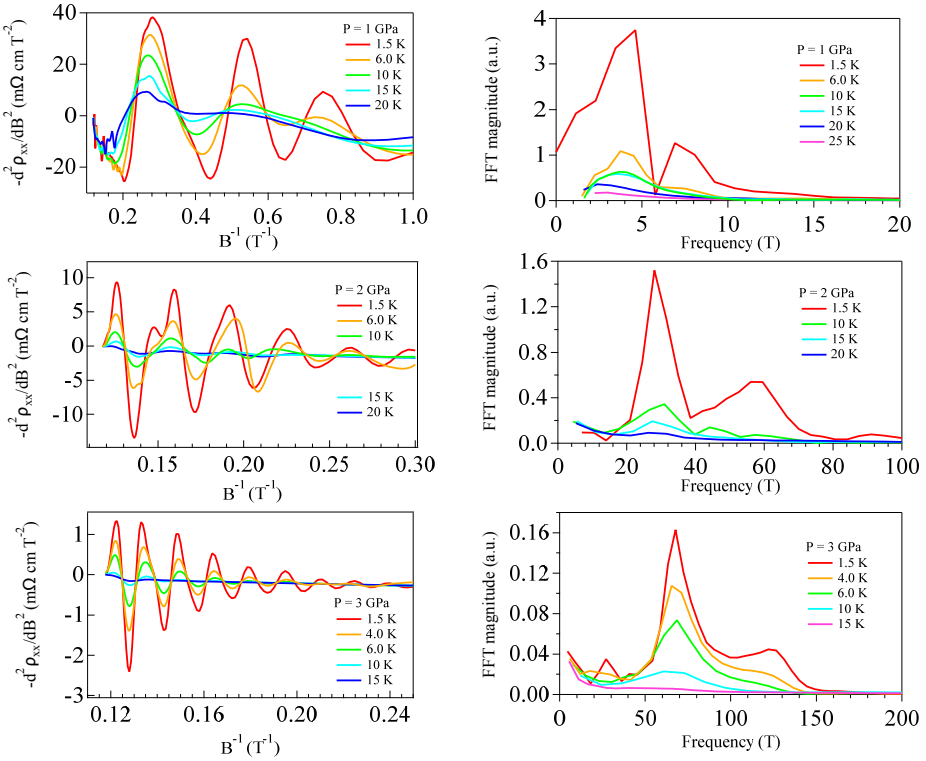

Fig. S5 (Color online) Temperature and field dependence of SdH oscillations (left column) and the result of fast Fourier transform (FFT) (right column) in the A17 phase at $P \leq 3$ GPa.

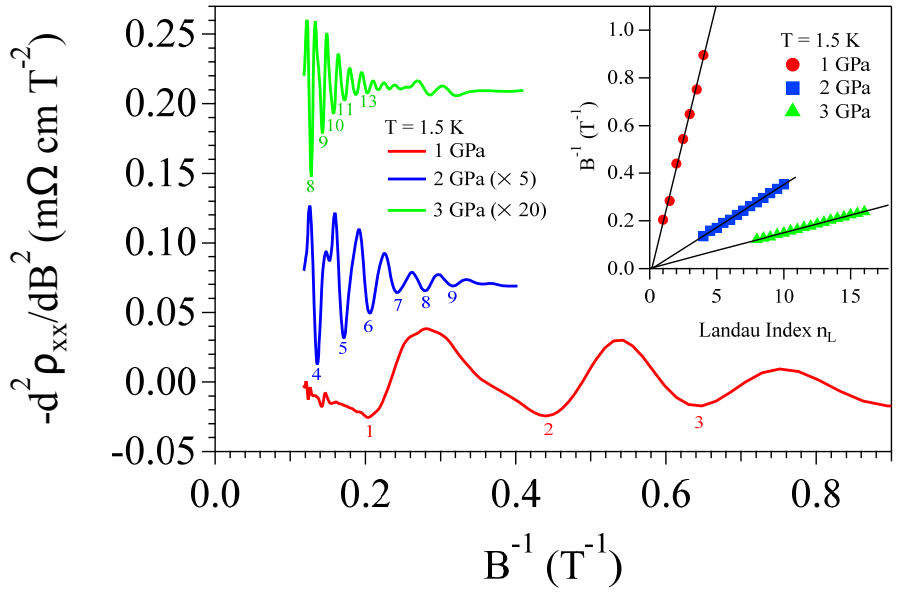

Fig. S6 (Color online) Quantum oscillations found at different pressures. The inset: nods of the quantum oscillations versus the Landau index.

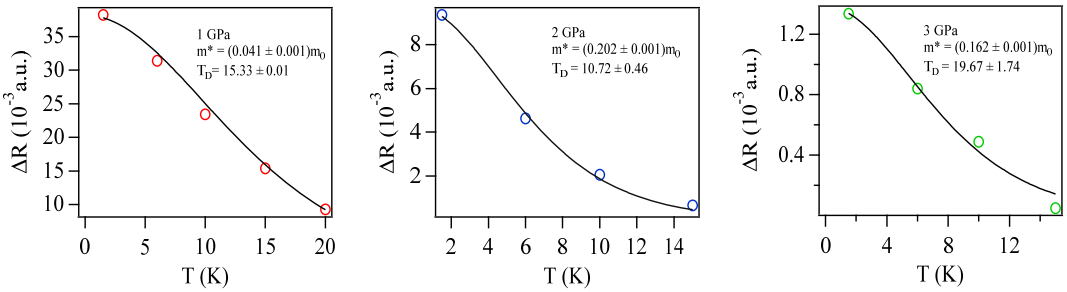

Fig. S7 (Color online) Best fitting to of the temperature dependence of the amplitude of the oscillation at different pressures.

5. Linear fitting at high fields of Hall resistivity ρ_{xy}

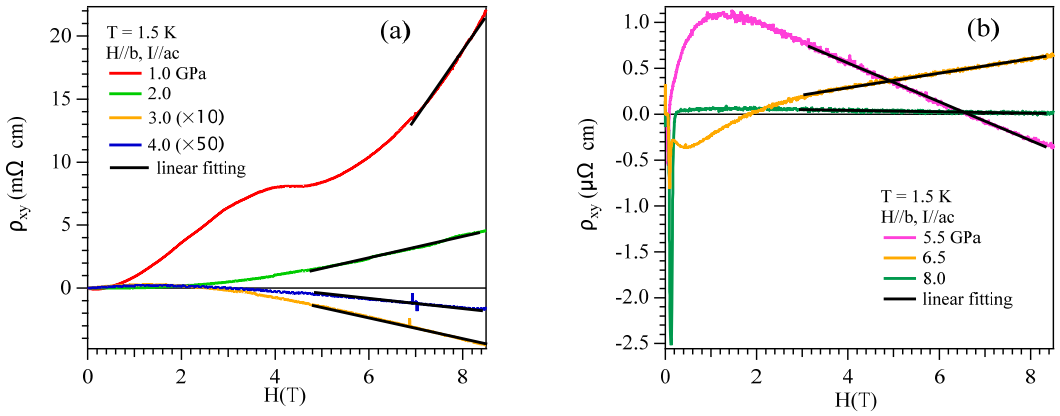

Fig. S8 (Color online) The goodness of linear fitting by $n_c \equiv \left|\frac{1}{eR_H}\right| = |n_h - n_e|$ to the high fields of ρ_{xy} at different pressures.

The results presented in Fig. S8 are quite different from those reported in the literature (6) in which a diamond anvil cell has been used. First of all, the limited sample size in the high pressure chamber of a DAC makes it very difficult to have an accurate measurement of Hall resistivity. Instead, the authors only presented the Hall resistance. In addition to the influence of a non-hydrostatic pressure effect as discussed at the beginning of the main text, the layer orientation change on crossing the A17 to A7 phase transition may contribute to the difference between two measured results. It is natural to believe an anisotropic Hall resistivity in the layered A17 and A7 phases. The layers in the A7 phase are formed 45º relative to that in the A17 phase. Therefore, the measurement configuration to probe the layer contribution in the A17 phase picks up some component between layers, which is related to the sample's thickness. We have used a much thicker flake of BP crystal than that used in the study with a DAC.

5. Superconductivity

In order to shed light on the non-monotonic pressure variations of T_c, we examined the temperature dependence of the critical field H_c determined from the $\rho(T)$ data under different magnetic fields as shown in Fig. S9. Here, we defined T_c as the zero-resistivity temperature. $H_c(T_c)$ follows the Ginzburg-Landau relation and the initial slope at T_c varies non-monotonically, as displayed in Fig. S10. Fig. S11 shows that the low-temperature region of zero-field resistivity for each pressure can be well fitted by the power law $\rho(T,0) = \rho_0 + AT^n$.

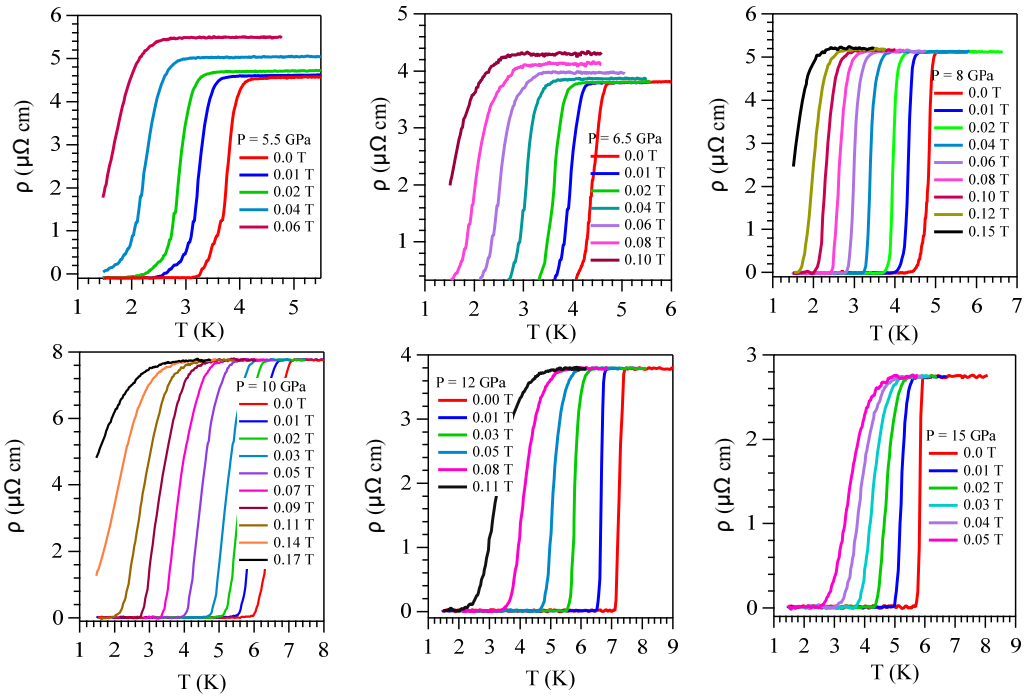

Fig. S9 (Color online) The field dependence of T_c at various pressures in the A7 and C phases.

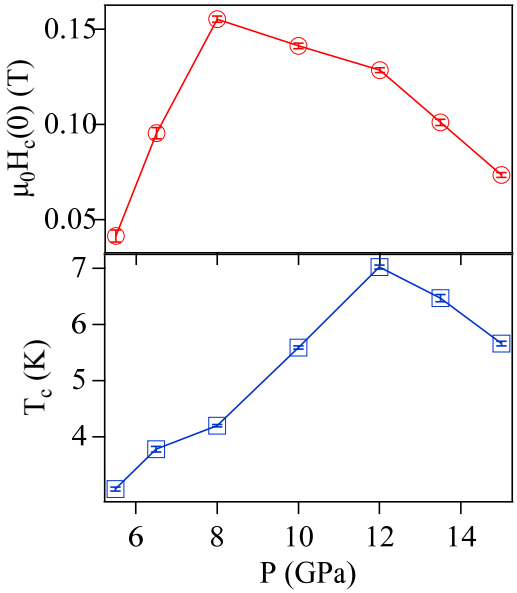

Fig. S10 (Color online) The evolution of critical field H_c and T_c under pressure.

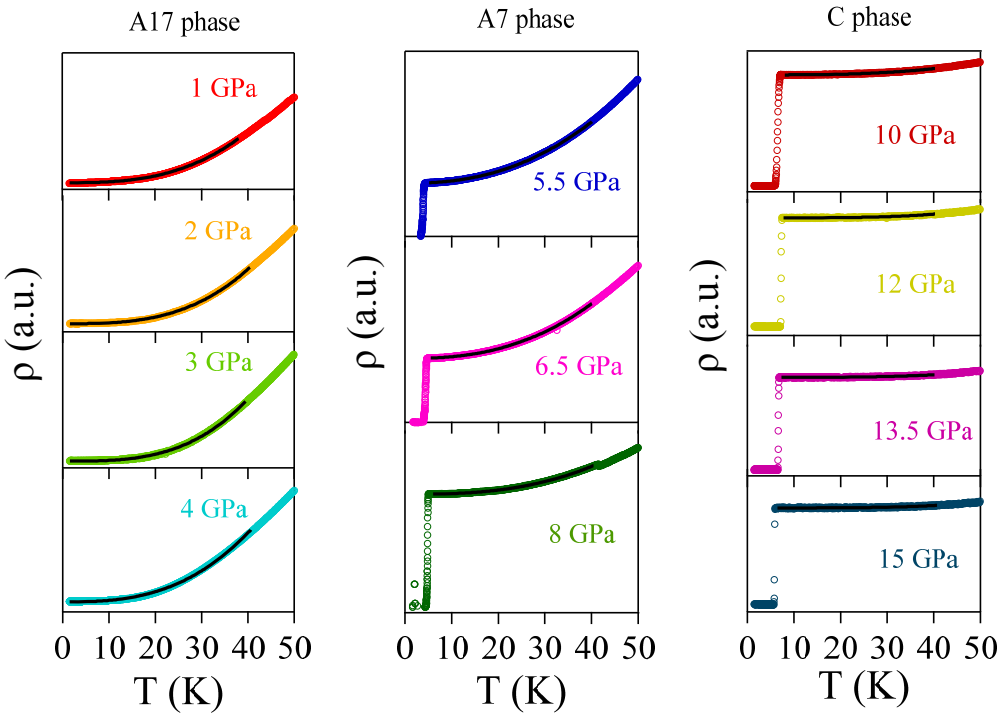

Fig. S11 (Color online) Fitting with the power law $\rho(T,0) = \rho_0 + AT^n$ (black solid lines) to the zero-field resistivity (color circles) at different pressures.

6. First-principles calculation

In our calculations the plane wave basis method is used (7). We adopt the generalized gradient approximation (GGA) with Perdew-Burke-Ernzerhof formula (8) for the exchange-correlation potentials. The norm-conserving pseudopotentials (9) are employed to model the electron-ion interactions. The kinetic energy cut-off and the charge density cut-off of the plane wave basis are chosen to be 80 Ry and 320 Ry, respectively. The charge density is calculated on a Γ-centered Brillouin-zone mesh of 24×24×24 points, with a Methfessel-Paxton smearing(10) of 0.02 Ry. The pressurized lattice constants are obtained from experiment. And then, the inner atomic positions are relaxed by minimizing the total energy. The phonons and the phonon perturbation potentials (11) are calculated on a Γ-centered 6×6×6 mesh, within the framework of density-functional perturbation theory(12).

Maximally localized Wannier functions (MLWFs) (13, 14) are constructed on a 6×6×6 grid of the Brillouin zone, using 8 random Gaussian functions as the initial guess. Fine electron (60×60×60) and phonon (30×30×30) grids are used to interpolate the electron-phonon coupling (EPC) quantities with Wannier90 (15) and EPW codes(16). Dirac δ-functions for electrons and phonons are replaced by smearing functions with widths of 45 and 0.2 meV, respectively. The EPC constant λ can be determined through summation

over the Brillouin zone or integration of the Eliashberg spectral function $\alpha^2F(\omega)$ in frequency space as(17, 18),

$$\lambda = \frac{1}{N_q}\sum_{qv}\lambda_{qv} = 2\int\frac{\alpha^2F(\omega)}{\omega}d\omega. \quad (1)$$

The EPC constant λ_{qv} for mode v at wavevector q is defined by(17, 18),

$$\lambda_{qv} = \frac{2}{\hbar N(0)N_k}\sum_{ijk}\frac{1}{\omega_{qv}}\left|g^{ij}_{k,qv}\right|^2\delta\left(\epsilon^i_q\right)\delta\left(\epsilon^j_{k+q}\right). \quad (2)$$

Here $g^{ij}_{k,qv}$ is the EPC matrix element, which describes the probability amplitude for scattering an electron with a transfer of crystal momentum $\mathbf{q}$. ij and v denote indices of energy bands and phonon modes, respectively. ω_{qv} stands for the phonon frequency of the v-th phonon mode with wavevector $\mathbf{q}$. ϵ^i_q and ϵ^j_{k+q} are eigenvalues of Kohn-Sham orbitals with respect to Fermi energy at given bands and momentums. $N(0)$ is the electronic density of states (DOS) at the Fermi energy. N_q/N_k is the total number of q/k points in the fine Brillouin-zone mesh. The Eliashberg spectral function can be expressed as(17, 18),

$$\alpha^2F(\omega) = \frac{1}{2}\sum_{qv}\delta\left(\omega-\omega_{qv}\right)\lambda_{qv}\omega_{qv}. \quad (3)$$

For a BCS superconductor, T_c can be expressed by the McMillian-Allen-Dynes formula (MAD) (18),

$$T_c = \frac{\omega_{log}}{1.2}exp\left[\frac{-1.04(1+\lambda)}{\lambda(1-0.62\mu^*)-\mu^*}\right]. \quad (4)$$

where $\mu^*$is the effective screened Coulomb repulsion constant, ω_{log} is the logarithmic average frequency, and the e-ph coupling constant λ is given by $\lambda = N(E_F)\langle I^2\rangle/M\langle\omega^2\rangle$, in which $N(E_F)$ is the electronic density of states at the Fermi level, $\langle I^2\rangle$ is the square of the electronic matrix element of the change of the crystal potential and $M\langle\omega^2\rangle$ stands for the atomic mass. Since the $N(E_F)$ and average e-ph interaction depend on the details and the topology of FS, we have calculated the band structures and FS of the A7 phase at P = 5.48 GPa (the lattice corresponds to 5.48 GPa in the experiment is used in the calculation) as shown in Fig. S12. There are two energy bands crossing the Fermi level forming a tetrahedral electron Fermi surface and hole pockets surrounding the center of hexagon, respectively. With further raising the pressure from 5.48 GPa, the valence band maximum increases, but the conduction band minimum decreases. As a consequence, the volumes that are enclosed by either electron or hole Fermi surfaces are enlarged, which is consistent with the carrier density change under high pressure in our experimental results. Compared to the band structures at P > 1 GPa in the A17 phase. (19) where the topological states form Dirac cones and massless fermions give rise to a small $N(E_F)$, the

most striking feature in the A7 phase is the almost flat bands near the Fermi level at **L** and **X** points of the Brillouin zone. A much enhanced $N(E_F)$ appears to be a primary factor leading to the emergence of superconductivity in the A7 phase. Furthermore, T_c and how it responds to pressure from experiments up to 6.7 GPa in the A7 phase can be reproduced with the MAD formula and the electron and phonon structures from first-principals calculation. However, a slight decrease of T_c for $P > 6.7$ GPa does not match a continuous increase with pressure from the experiment.

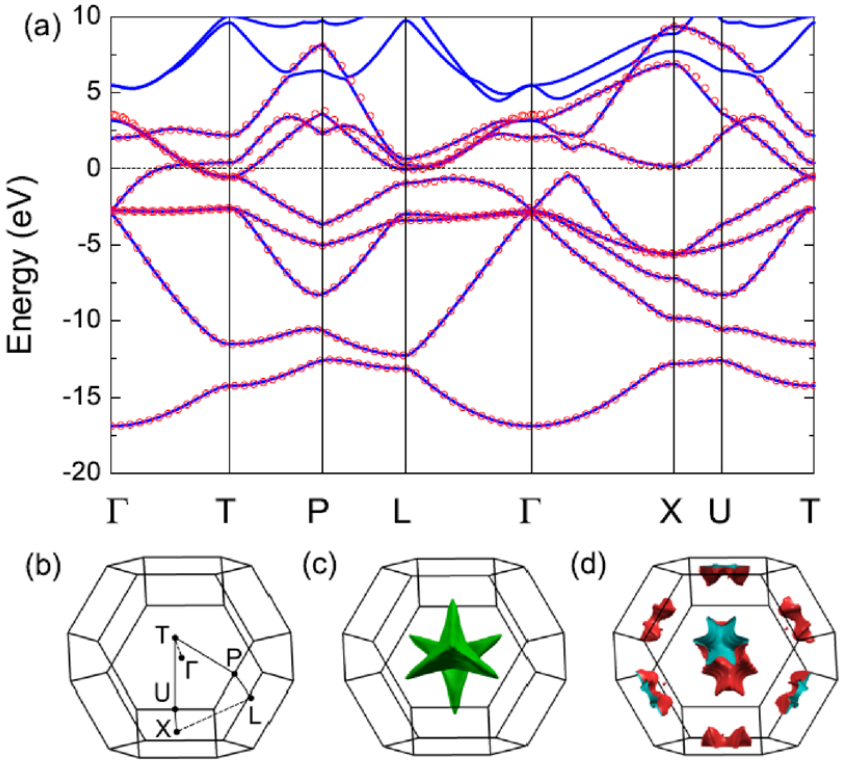

Fig. S12 (Color online) Band structures and Fermi surfaces of black phosphorus in the A7 phase under 5.48 GPa. (a) Fermi level is set to zero. The solid blue lines represent band structures given by a first principle calculation. The red circles denote band structures obtained from the interpolation of maximally localized Wannier functions (MLWFs); (b) high-symmetry points in the Brillouin zone; (c) tetrahedral electron Fermi surfaces; (d) hole pockets surrounding the center of hexagon.

The band structure obtained by interpolation of MLWFs exhibits excellent agreement with the first-principles one below 3.0 eV. The electronic Hamiltonian, dynamical matrix, and EPC matrix element in the Wannier representation show exponential decay (Fig. S13), which further guarantees the reliability of subsequent Wannier interpolation.

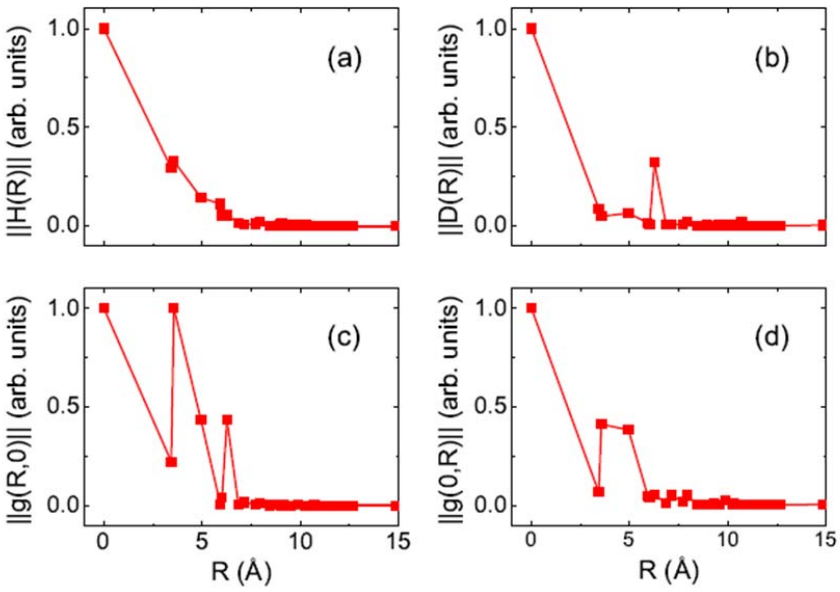

Fig. S13 (Color online) Spatial decays of the electronic Hamiltonian $\|H(R)\|$, the dynamical matrix $\|D(R)\|$ and the EPC matrix element $\|g(R,0)\|$ and $\|g(0,R)\|$ in the Wannier representation of black phosphorus in the A7 phase under 5.48 GPa.

Up to 9.62 GPa, no imaginary frequency is found in the phonon spectra, indicating the dynamical stability of the A7 phase. This is consistent with the critical pressure of 10 GPa for the structural phase transition from the A7 to the C phase (20). The separation between acoustic phonon branches and the optical ones results in a gap in phonon DOS $F(\omega)$ (Fig. S14). Upon applying pressure, the acoustic phonon branches show obvious hardening, while the impact of pressure on the optical phonons is relatively small. We also find that the Eliashberg spectral function $\alpha^2F(\omega)$ has two broadening peaks. Moreover, the similarity between $\alpha^2F(\omega)$ and $F(\omega)$ suggests that the strength of EPC matrix element around the Fermi level is close to each other.

By setting μ^* to 0.17, the superconducting transition temperatures at 5.48 and 6.71 GPa are in accord with experimental measurement (see Table SI). But in comparison to the monotonically increasing behavior of T_c versus pressure in experiment, there is an abnormal descend for the calculated T_c at 8.38 GPa. From the theoretical point of views, this can be attributed to the hardening of acoustic phonon modes and blue shift of the first peak in $\alpha^2F(\omega)$ (Fig. 14). Since the $\lambda(\omega)$ for 8.38 GPa begins to diverge with respect to that of 6.71 GPa at about 20 meV (Fig. 14(e)). The discrepancy in T_c between experiment and theoretical calculation may be attributed to (a) μ^* is an empirical parameter; its variation under pressure has not been taken into consideration; and (b) in the simulation of layered structure (such as the A7 phase of black phosphorus), the van der Waals correction should be properly included.

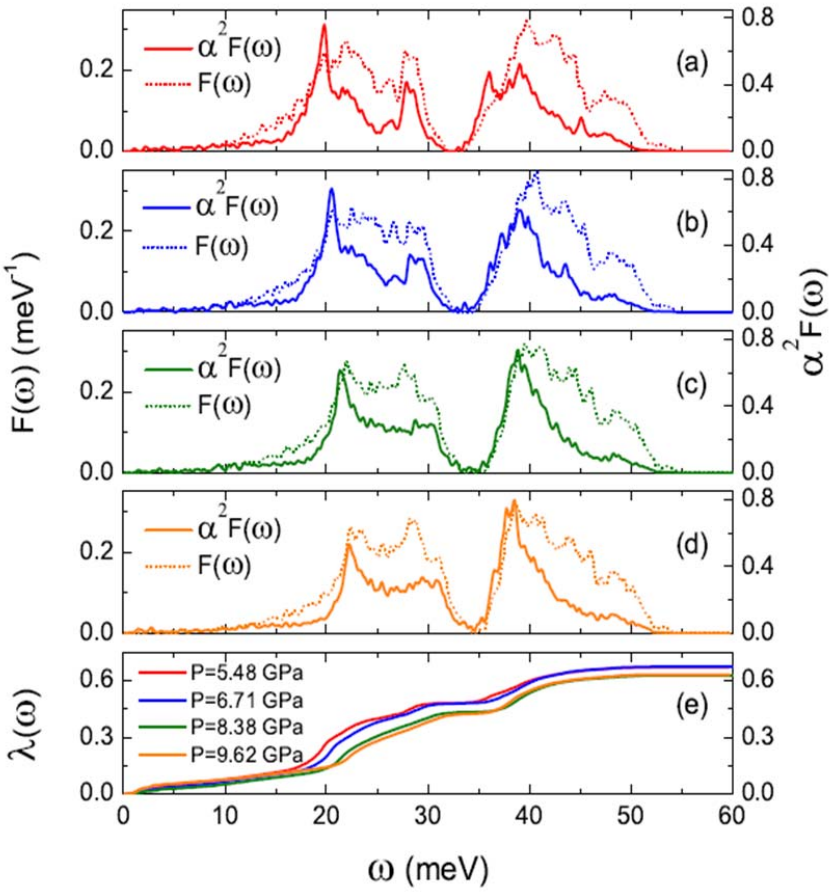

Fig. S14 (Color online) (a)-(d) Phonon DOS $F(\omega)$ and Eliashberg spectral function $\alpha^2F(\omega)$ for black phosphorus in the A7 phase under different pressures specified in (e); (e) $\lambda(\omega)$, which is defined by $2\int_0^{\omega}\frac{1}{\omega'}\alpha^2F(\omega')d\omega'$.

Table SI Calculated EPC constant λ, $\log\omega$ and T_c under different pressures. The μ^* is chosen to be 0.1 and 0.17 for comparison.

P (GPa)	λ	$\omega_{\log}$ (meV)	T_c (K)	
			$\mu^* = 0.1$	$\mu^* = 0.17$
5.48	0.669	20.15	7.3	3.4
6.71	0.673	21.66	7.9	3.7
8.38	0.627	23.30	7.1	3.0
9.62	0.633	21.40	6.6	2.8

1. Li X, Yan J-Q, Singh DJ, Goodenough JB, & Zhou J-S (2015) Synthesis of monoclinic IrT e 2 under high pressure and its physical properties. *Physical Review B* 92(15):155118.
2. Cheng J-G*, et al.* (2014) Integrated-fin gasket for palm cubic-anvil high pressure apparatus. *Review of Scientific Instruments* 85(9):093907.
3. Goldsmid H & Sharp J (1999) Estimation of the thermal band gap of a semiconductor from Seebeck measurements. *Journal of electronic materials* 28(7):869-872.
4. Li L*, et al.* (2014) Black phosphorus field-effect transistors. *Nature nanotechnology* 9(5):372.
5. Zhu Z & Tománek D (2014) Semiconducting layered blue phosphorus: a computational study. *Physical review letters* 112(17):176802.
6. Guo J*, et al.* (2017) Electron-hole balance and the anomalous pressure-dependent superconductivity in black phosphorus. *Physical Review B* 96(22):224513.
7. Giannozzi P*, et al.* (2009) QUANTUM ESPRESSO: a modular and open-source software project for quantum simulations of materials. *Journal of Physics: Condensed Matter* 21(39):395502.
8. Perdew JP, Burke K, & Ernzerhof M (1996) Generalized gradient approximation made simple. *Physical review letters* 77(18):3865.
9. Troullier N & Martins JL (1991) Efficient pseudopotentials for plane-wave calculations. *Physical Review B* 43(3):1993.
10. Methfessel MPAT & Paxton AT (1989) High-precision sampling for Brillouin-zone integration in metals. *Physical Review B* 40(6):3616.
11. Giustino F, Cohen ML, & Louie SG (2007) Electron-phonon interaction using Wannier functions. *Physical Review B* 76(16):165108.
12. Baroni S, De Gironcoli S, Dal Corso A, & Giannozzi P (2001) Phonons and related crystal properties from density-functional perturbation theory. *Reviews of Modern Physics* 73(2):515.
13. Marzari N & Vanderbilt D (1997) Maximally localized generalized Wannier functions for composite energy bands. *Physical Review B* 56(20):12847.
14. Souza I, Marzari N, & Vanderbilt D (2001) Maximally localized Wannier functions for entangled energy bands. *Physical Review B* 65(3):035109.
15. Mostofi AA*, et al.* (2008) wannier90: A tool for obtaining maximally-localised Wannier functions. *Computer physics communications* 178(9):685-699.
16. Noffsinger J*, et al.* (2010) EPW: A program for calculating the electron–phonon coupling using maximally localized Wannier functions. *Computer physics communications* 181(12):2140-2148.
17. Allen PB (1972) Neutron spectroscopy of superconductors. *Physical Review B* 6(7):2577.
18. Allen PB & Dynes RC (1975) Transition temperature of strong-coupled superconductors reanalyzed. *Physical Review B* 12(3):905.
19. Li C-H*, et al.* (2017) Pressure-induced topological phase transitions and strongly anisotropic magnetoresistance in bulk black phosphorus. *Physical Review B* 95(12):125417.
20. Kikegawa T & Iwasaki H (1983) An X-ray diffraction study of lattice compression and phase transition of crystalline phosphorus. *Acta Crystallographica Section B: Structural Science* 39(2):158-164.